Acta Biomaterialia 7 (2011) 83–95

Contents lists available at ScienceDirect

Acta Biomaterialia

journal homepage: www.elsevier.com/locate/actabiomat

Biomechanics of brain tissue

Thibault P. Prevost [a], Asha Balakrishnan [b], Subra Suresh [a,b,c], Simona Socrate [c,*]

[a] Department of Materials Science and Engineering, Massachusetts Institute of Technology, Cambridge, MA 02139, USA
[b] Department of Mechanical Engineering, Massachusetts Institute of Technology, Cambridge, MA 02139, USA
[c] Harvard–MIT Division of Health Sciences and Technology, Massachusetts Institute of Technology, Cambridge, MA 02139, USA

ARTICLE INFO

Article history:
Received 16 February 2010
Received in revised form 28 June 2010
Accepted 29 June 2010
Available online 21 August 2010

Keywords:
Brain tissue mechanics
Nonlinear dynamic behavior
Visco-hyperelastic
Bulk response
High rate

ABSTRACT

The dynamic behavior of porcine brain tissue, obtained from a series of in vitro observations and experiments, is analyzed and described here with the aid of a large strain, nonlinear, viscoelastic constitutive model. Mixed gray and white matter samples excised from the superior cortex were tested in unconfined uniaxial compression within 15 h post mortem. The test sequence consisted of three successive load–unload segments at strain rates of 1, 0.1 and 0.01 s^{-1}, followed by stress relaxation ($n = 25$). The volumetric compliance of the tissue was assessed for a subset of specimens ($n = 7$) using video extensometry techniques. The tissue response exhibited moderate compressibility, substantial nonlinearity, hysteresis, conditioning and rate dependence. A large strain kinematics nonlinear viscoelastic model was developed to account for the essential features of the tissue response over the entire deformation history. The corresponding material parameters were obtained by fitting the model to the measured conditioned response (axial and volumetric) via a numerical optimization scheme. The model successfully captures the observed complexities of the material response in loading, unloading and relaxation over the entire range of strain rates. The accuracy of the model was further verified by comparing model predictions with the tissue response in unconfined compression at higher strain rate (10 s^{-1}) and with literature data in uniaxial tension. The proposed constitutive framework was also found to be adequate to model the loading response of brain tissue in uniaxial compression over a wider range of strain rates (0.01–3000 s^{-1}), thereby providing a valuable tool for simulations of dynamic transients (impact, blast/shock wave propagation) leading to traumatic brain injury.

1. Introduction

The study of the mechanical properties of brain matter – at the tissue continuum level – has been the focus of numerous investigations in the past four decades (see for example [1–7]). Many investigators have concentrated their effort on characterizing the coupled time and strain/stress dependencies inherent in the response of the tissue to externally applied mechanical transients, e.g. frontal or lateral impact on the head by a rigid mass [8–10], linear or angular acceleration pulses applied to the skull [11,12] or indentation of the cortex surface [13]. Understanding how these loading/kinematic conditions applied to the organ boundary translate into local stress–strain states within the tissue continuum is challenging, because the brain is, from a biomechanical perspective, a highly complex organ housing multiple "substructures", e.g. brainstem, cerebellum, thalamus, cerebral cortex, corpus callosum, associated with somewhat distinct mechanical properties [14–16]. Most biomechanical studies have been conducted in vitro, although a few measurements have also been reported in vivo [17–21]. The results of different studies are at times difficult to reconcile, due to the wide range of variation in experimental protocols, including the species/age of the subjects (human, porcine, bovine or murine), the loading configurations (compression, shear, tension or indentation), the loading histories (cyclic, stress relaxation or creep) and test regime (small/large strains or low/high strain rates). The collected data have facilitated the development of a large variety of constitutive models, some of which have been shown to account for essential features of the tissue response [22–24] under selected test conditions. Nonetheless, the integration of all the characteristic features of the large strain tissue response (hysteretic behavior, rate dependence, nonlinearity, shear and volumetric behavior) into one single constitutive framework has not been achieved thus far.

This study is a component of a multidisciplinary effort aimed at elucidating some key effects of primary blast on the central nervous system [25] and represents a first step towards the development of a predictive model for the response of brain tissue over an extensive range of strains and strain rates. A parallel effort is underway to assess differences between tissue properties under in vivo and in vitro conditions, where the proposed constitutive formulation is employed to analyze the results of indentation tests

---

* Corresponding author. Tel.: +1 617 452 2689.
E-mail address: ssocrate@mit.edu (S. Socrate).

1742-7061/$ - see front matter © 2010 Acta Materialia Inc. Published by Elsevier Ltd. All rights reserved.
doi:10.1016/j.actbio.2010.06.035

performed with a custom dynamic tool [26]. The first section of this paper describes the experimental component of the study (test protocols and main results gathered on porcine cortical samples), while the second section addresses the modeling effort (constitutive laws, numerical implementation, model validation and predictions). Both are preceded by a brief literature review. Some of the limitations inherent in the current model formulation are discussed in the last section, guiding the effort for future model refinements. This paper constitutes a preliminary step in the development of a comprehensive experimental database and enhanced computational tools to be employed in support of a variety of clinical applications, as well as to elucidate mechanically mediated pathways leading to traumatic brain injury.

2. Experiments

2.1. Literature review

Mechanical tests on brain samples have been conducted mainly in the linear regime via small oscillatory deformations imposed on the tissue, in pure shear or in torsion, over a wide spectrum of frequencies [27–30]. In assessing the time/frequency dependence of the linear viscoelastic properties of the tissue (i.e. storage and loss moduli), these studies have uncovered some important aspects of the tissue dynamics. The thrust of the results reported, nonetheless, suffers from a few limitations. First, most of the data so gathered lack consistency, in that the magnitude of the measured scalar moduli varied at times by more than 10-fold in relative terms from one study to another [31]. This lack of consistency may be attributed to multiple factors, including: inter-species/intra-species variations (e.g. animal breed, age, sex and inherent biological variability); differences in (1) post mortem testing time, (2) tissue storage and hydration conditions, (3) tissue preparation/excision methods, (4) specimen neuroanatomical orientation, (5) temperature conditions, (6) interfacial testing conditions (degree of tissue friction/adherence/slipping on the test fixtures) and (7) pre-conditioning effects prior to actual testing. Further, the scope of these investigations was limited per se to small deformations, as the tissue had been shown to deviate from linearity at strains greater than 1% [32,33]. More recently, the nonlinear features of the tissue response have been partly characterized in compression [34,35], tension [36] and shear [23,37]. While some of these studies measured the tissue response over more than two orders of strain rate magnitude, they were mostly focused on a limited set of test histories (e.g. single load ramp and stress relaxation tests or sinusoidal load–unload cyclic tests at low to medium strains), excluding any direct assessment of the tissue volumetric behavior. Some attempts have been made to retrieve quantitative information on the tissue volumetric compliance [38,39], but these attempts remain scarce and limited in scope, most investigators relying on incompressibility assumptions or speculative arguments [34,40,41]. The experimental part of this study aimed to address some of the limitations noted in previous investigations via the systematic collection of experimental data on porcine cortical specimens in unconfined uniaxial compression comprising the following measurements: (1) nonlinear strain and strain rate dependencies in load and unload over three orders of strain rate magnitude (0.01–1 s^{-1}) in the large deformation regime (up to 50% nominal strain); (2) long-term time dependencies in relaxation; (3) lateral tissue deformation to assess volumetric compliance. A porcine model was preferred to other animal models because its gyrencephalic brain, architecturally close to the human brain, has been proven to share with the latter some similarities in terms of pre- and postnatal cerebral development relative to tissue growth, myelination and composition [42–46]. Swine models constitute, moreover, an affordable alternative to more costly, ethically sensitive primate models.

2.2. Test protocol – unconfined uniaxial compression in vitro

2.2.1. Specimen preparation

Sixteen 6- to 18-month-old swine brains (female, Yorkshire breed) were obtained from a local vendor (Research 87 Inc., Boylston, MA), following a protocol approved by the Committee on Animal Care at the Massachusetts Institute of Technology. Pigs having reached at least six months of age may be considered cerebrally mature [42] and were therefore selected to minimize age-related variability (neonatal pigs have been shown to have significantly softer brains [31]). The brains were sectioned along the mid-sagittal plane and transferred on ice to the laboratory within 3 h post mortem. Each hemisphere was rinsed upon delivery in phosphate-buffered saline (PBS, 10 mM phosphate buffer) and kept refrigerated in solution to limit tissue degradation. Shortly before testing mixed gray and white matter samples were excised from the superior cortical region (frontal and parietal lobes) and maintained hydrated in PBS during all subsequent steps. No notable differences were observed in mechanical properties between the two cortical regions. This observation complements findings previously reported by Coats and Margulies [47] on local cortical gray matter homogeneities at the subcentimetric/millimetric tissue level. Preliminary investigations of the optimal sample size for uniaxial compression tests [48] showed that large samples, in the cubic centimeter range, yielded the most consistent results. All the data collected for this study were therefore obtained from samples that were approximately, 25.4 × 25.4 mm in cross-section and 9 mm in thickness (Fig. 1A). The mechanical properties obtained shall be viewed as "homogenized" properties of the superior cortex (gray and white matter combined), although the samples tested were composed predominantly of gray matter, accounting typically for ~70% of the sample mass. The experimental protocols were primarily designed so as to reduce the sources of experimental variability arising from tissue handling, which are many, given the delicate nature of the brain parenchyma. Separating intermingled gray and white matter of the superior cortex was ill-suited to this study because the separation/cutting process implied further alterations in the tissue virgin state (via shearing or stretching) which were deemed too costly relative to the potential benefits.

2.2.2. Axial and lateral measurements

The samples ($n = 25$ from $N = 16$ Yorkshire sows) were tested in unconfined uniaxial compression on commercial testing machines equipped with 20 N load cells (ElectroForce 3200, Bose Corp., Framingham, MN ($n = 11$); Zwick Z2.5/TS1S, Ulm, Germany ($n = 14$)). Prior to testing the platens were humidified with PBS to minimize friction at the tissue–platen interface. All tests were conducted at room temperature ($T = 21$ °C). Samples were tested between 4 and 15 h post mortem, with no significant variations in tissue response being noted in relation to post mortem test time differences. The responses measured were also found to be comparable with those reported by Tamura et al. [35], who conducted similar tests within a shorter time frame post mortem (see Section 3). A preload of 0.02 N (corresponding to a compressive stress of ~30 Pa) was imposed on each sample prior to testing in order to accurately determine the sample thickness. Each sample was subjected to a sequence of three loading segments, at nominal strain rates of 1, 0.1 and 0.01 s^{-1}, respectively, each comprising five load–unload cycles to 50% nominal strain, followed by a ramp relaxation segment to 50% nominal strain held for 300 s with a ramp rate of 1 s^{-1}. Fig. 1 illustrates the imposed strain history (Fig. 1C) and the resulting stress history (Fig. 1D) for one representative tissue specimen. The transverse displacements were captured

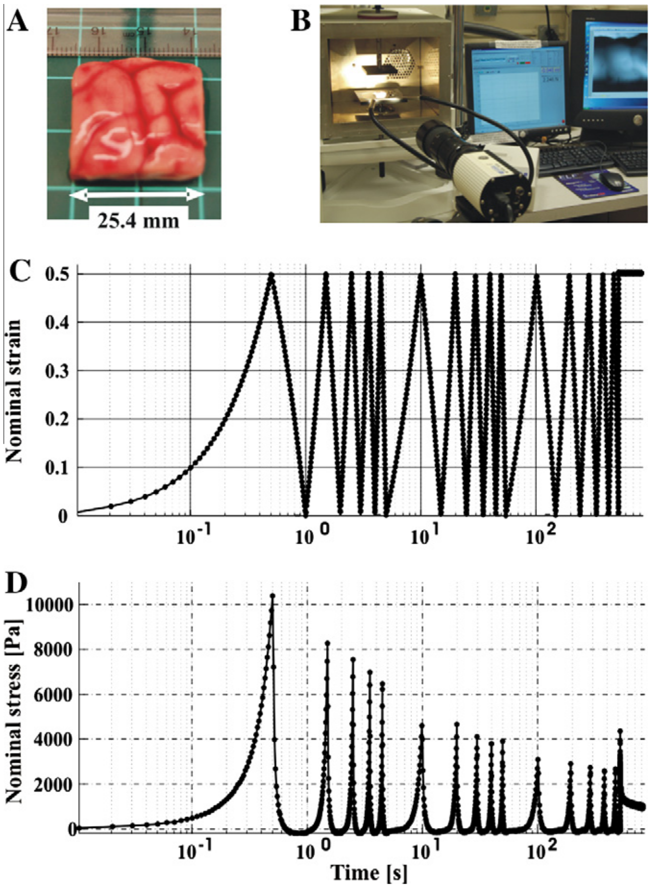

Fig. 1. Experimental protocol. (A) Cortical tissue sample. (B) Optical extensometry. (C) Imposed strain history (logarithmic time scale). Each sample was subjected to a sequence of three loading segments, at 1, 0.1 and 0.01 s^{-1} nominal strain rates, respectively, each comprising five load–unload cycles to 50% nominal strain, followed by a ramp relaxation segment to 50% nominal strain held for 300 s with a ramp rate of 1 s^{-1}. (D) Resulting stress history for a representative tissue sample.

by a Qimaging Retiga 1300 CCD camera equipped with a 200 mm f/4 Nikon lens (Fig. 1B). Lateral stretch measurements were deemed sufficiently accurate only for a subset of specimens ($n = 7$), because most samples had somewhat irregular edges. Axial data (force and displacement) and lateral deformation images were acquired synchronously via Vic-Snap software (v. 3.0D, Correlated Solutions Inc.). The lateral stretches were subsequently assessed using a MATLAB custom image analysis routine. The processed data are shown for one representative specimen in Fig. 2. Note that the nominal axial strain values reported in Figs. 1 and 2 are based on the platen axial displacement history. In practice, most of the specimens did not entirely recover their initial configuration upon unloading: as the platens traveled back to their initial position at the end of each load–unload cycle the degree of adhesion between the platen and the specimen was often insufficient to enforce complete recovery of the original specimen height. Full contact was re-established at the beginning of the subsequent loading ramps (with a rise in the recorded load) and was lost at the end of the unloading ramps (as the load became negative, tracking the weak tensile adhesive forces between the top surface of the specimens and the platen).

2.3. Results

Stress–strain diagrams have been extracted from the representative data in Fig. 1 for the three load–unload segments (at 1, 0.1 and 0.01 s^{-1}) and are plotted in Fig. 3, together with the subsequent relaxation response. As shown in Fig. 3, the tissue behavior in unconfined compression was intrinsically nonlinear at finite deformation, in both the strain and strain rate domains. The tissue response exhibited marked hysteretic features over the range of strain rates considered for this study. Another notable feature was the substantial degree of "conditioning" associated with the first loading ramp, i.e. the dramatic increase in tissue compliance between the initial loading cycle and the subsequent cycles. Differences associated with softening effects between sequential ("conditioned") cycles at the same loading rate were much less dramatic. Conditioning effects reflected changes in tissue "state" occurring during the first cycle of loading through which the tissue may lose part of its interstitial fluid and/or undergo "irrecoverable" microstructural reorganization/reconfiguration (damage). To ascertain if conditioning was associated with a permanent change in tissue properties, a study was performed on a subset ($n = 6$) of tissue samples which were submitted to two series of five load–unload cycles (uniaxial compression to 50% nominal strain at 1 s^{-1}) separated by a 2 h recovery period in PBS. To a large extent, the rehydrated samples recovered their original response, with conditioning patterns highly similar to those measured on the virgin tissue, as illustrated in Fig. 4 for one representative tissue

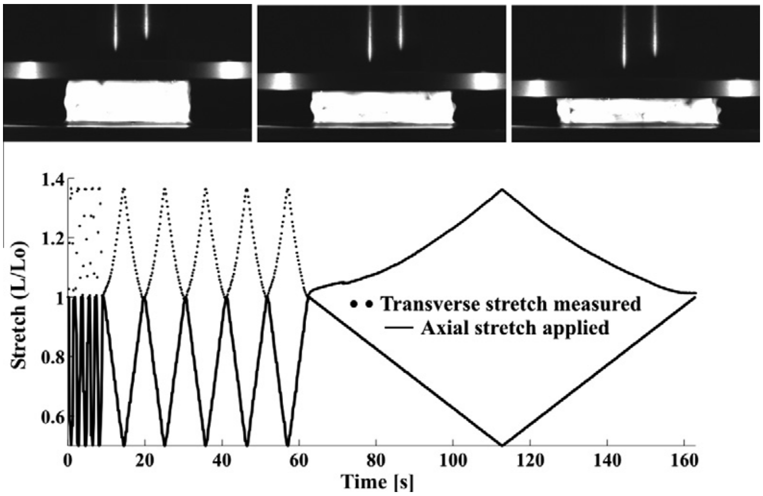

Fig. 2. Images of the tissue sample at increasing levels of axial deformation. The lateral stretch measurements were obtained by visual extensometry.

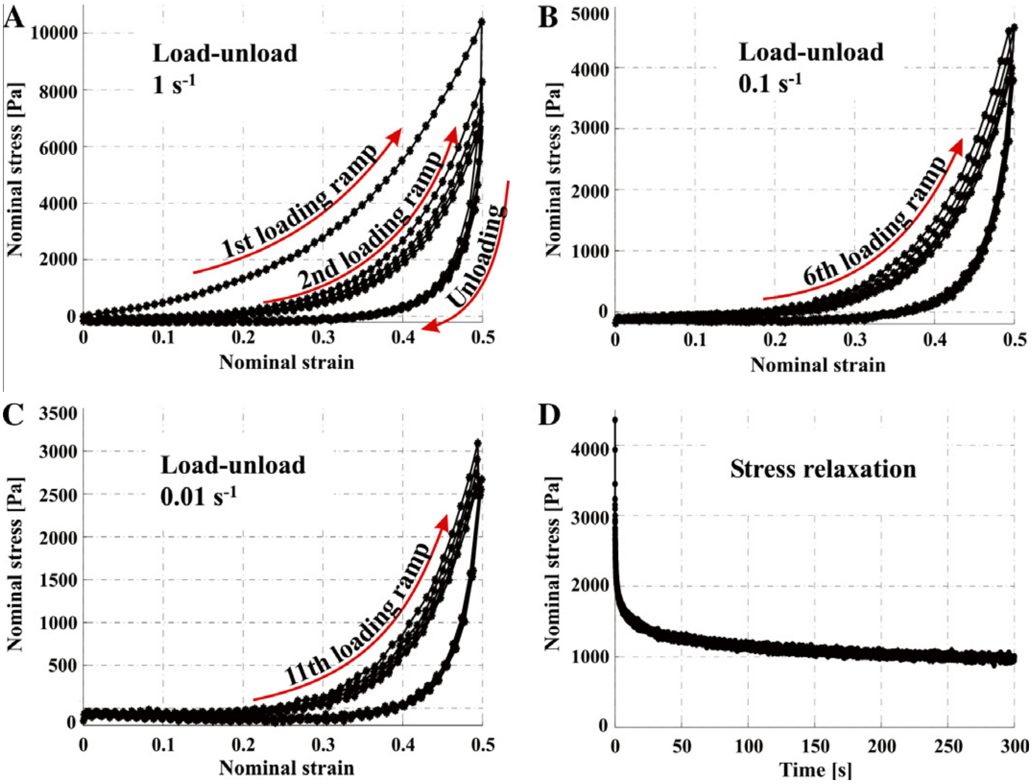

Fig. 3. Representative cortical tissue response in unconfined compression. Data in panels (A)–(D) were obtained sequentially on the same tissue sample (see the corresponding strain/stress time histories for this representative sample in Fig. 1C and D).

sample. This observation substantiates the hypothesis that interstitial fluid diffusion plays a crucial role in the conditioning process and that the tissue did not undergo substantial permanent damage in the first loading cycle. The essential features of the tissue response to the uniaxial compression loading protocol in Fig. 1 were found to be consistent for all tested samples. The average responses and standard deviations are shown in Fig. 5A and B (nominal axial stress) and in Fig. 5D (transverse stretch). For clarity purposes, the stress–strain plots only display the first (virgin) loading ramp at 1 s^{-1}, the subsequent (conditioned) loading ramp at 1 s^{-1} and the first (conditioned) loading ramps at 0.1 and 0.01 s^{-1}. The tissue response exhibited substantial volumetric compliance, with an average 12% volume reduction at an axial stretch of 0.5: $\Delta V/V^0 = -12 \pm 5.5\%$ ($N = 7$ samples, $n = 7 \times 6$ volumetric measurements taken from the sequences of load–unload cycles at 0.1 (×5) and 0.01 s^{-1} (×1) strain rates). Data previously published by Tamura et al. [35] for similar mixed gray/white matter samples from swine cortices are also shown in Fig. 5A. The (virgin) loading response measured in the Tamura study for a strain rate of 1 s^{-1} was found to be in good agreement with the results of the current study. Miller and Chinzei [34] also investigated the quasi-static response of similar tissue samples for the same animal model. The responses of virgin specimens measured by Miller and Chinzei at a strain rate of 0.64×10^{-2} s^{-1} are gathered in Fig. 5C and they were found to be significantly stiffer than the average (conditioned) response measured at a comparable strain rate (10^{-2} s^{-1}) in the present study. An exploratory set of measurements was performed to confirm that this discrepancy might be primarily attributed to conditioning effects. Virgin tissue samples ($n = 6$) were subjected to five load–unload cycles at a strain rate of 10^{-2} s^{-1}. The corresponding average first (virgin) loading response, shown in Fig. 5C, was found to be comparable with that reported by Miller and Chinzei.

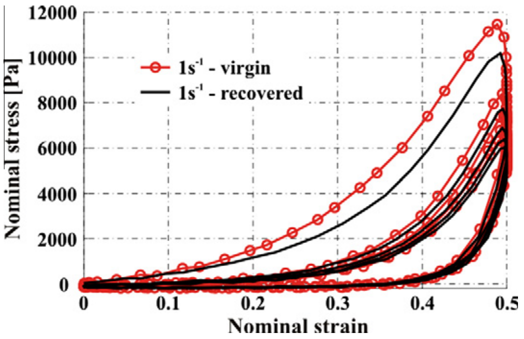

Fig. 4. Representative cortical tissue response in unconfined compression. The sample was submitted to two series of five load–unload cycles at 1 s^{-1} strain rate separated by a 2 h recovery phase in PBS.

3. Constitutive model

3.1. Literature review

Whether the brain should be considered, for continuum modeling purposes, as a single phase viscous solid or as a dual phase fluid-saturated solid is still the subject of differing viewpoints. The traditional dual phase approach follows the theory of consolidation (poroelasticity) originally formalized by Biot in the context of soil mechanics [49]. Although interstitial fluid diffusion and related transport mechanisms have long been recognized to play a crucial role in brain function [50], the poroelastic approach has received only marginal attention in the brain tissue biomechanics community [22,51]. In the single phase approach, dissipation mechanisms and time dependencies in the tissue response are addressed in the framework of viscoelasticity. Most of the models following this approach are adaptations or combinations of three

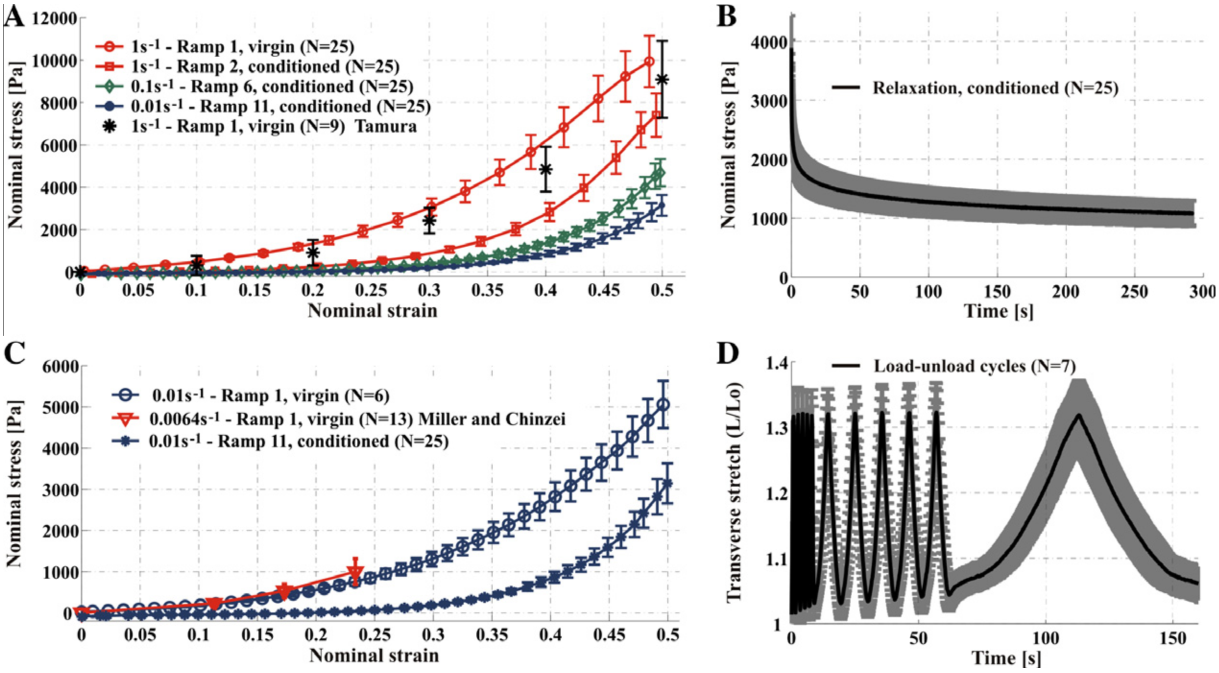

Fig. 5. Average tissue response and standard deviations. (A) Loading ramps at 1, 0.1 and 0.01 s^{-1}. (B) Relaxation. (C) Conditioning effects for the loading ramps at 0.01 s^{-1}. (D) Transverse stretch history for the load–unload cycles.

model subcategories: (1) linear viscoelastic models, based on cyclic loading, in which the tissue response is described by a set of two parameters, the storage and loss moduli [13,28–30]; (2) small strain formulations for rheological models based on linear or nonlinear spring–dashpot combinations [52,53]; (3) large strain kinematics quasilinear or nonlinear viscoelastic models for which the tissue response is decomposed into a hyperelastic component (neo-Hookean, Mooney–Rivlin or Ogden formulations are most common) and a dissipative component, e.g. multi-mode Prony series [5,22–24,54–56]. The linear and quasilinear models, mostly relevant in the small strain regime, are unable to fully capture the complexities of the tissue response at finite strains. In contrast, some of the large strain kinematics models, integrating nonlinearities within their formulation, have been able to successfully reproduce some specific features of the tissue deformation over fairly complex loading histories. Hrapko et al. [23] employed a multi-mode Mooney–Rivlin viscoelastic network in parallel with a nonlinear hyperelastic resistance to capture the simple shear responses of white matter in load, unload and relaxation at strain rates of 1–1.5 s^{-1} up to 50% strain, using 16 material parameters. More recently, El Sayed et al. [24] developed a nonlinear elastic-viscoplastic formulation to capture some of the hysteretic and dissipative characteristics of the tissue response in uniaxial tension and compression up to 50% nominal strain. The generalized framework proposed by El Sayed et al., in which an arbitrary number of viscoelastic networks are considered in parallel with a viscoplastic network, allowed the authors to fit a number of experimental findings with different configurations and numbers of constitutive elements. In most instances the phenomenological models proposed in the literature rely on a fairly large number of material parameters validated over a limited range of loading regimes/histories.

The nonlinear visco-hyperelastic model developed here is also phenomenological in nature; it espouses the modeling “philosophy” pursued by previous investigators and it idealizes the tissue as a single, homogeneous, isotropic phase. The proposed formulation combines the following advantages within a single framework: (1) it accounts for all the observed complexities inherent in the tissue response at low to medium strains and strain rates (i.e. nonlinearities, hysteresis, time-dependencies, volumetric behavior); (2) it is accurate and predictive over an extended range of strains and strain rates while requiring a relatively small number of material parameters; (3) it relies on physically motivated arguments, where different constitutive elements of the model, and their corresponding parameters, can be conceptually

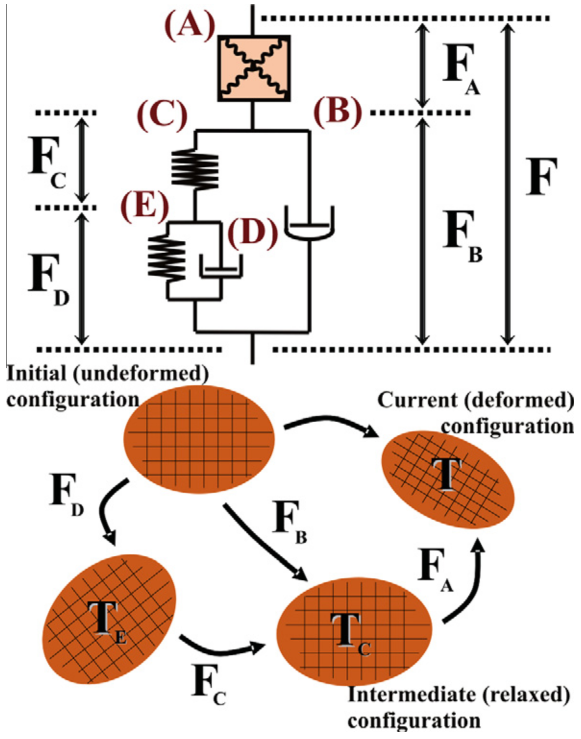

Fig. 6. Schematic of the rheological model (top) and corresponding large kinematics deformation map (bottom).

associated with specific underlying mechanisms of deformation. This empirical interpretation of modeling elements provides some guidance in the fitting process, as discussed in Appendix A.

3.2. Constitutive laws

A schematic (rheological) representation of the proposed model for the tissue response is shown in Fig. 6, with the corresponding 3D large kinematics deformation map. For the most part the notation used hereafter is that prevailing in modern continuum mechanics:

$\mathbf{F}_\bullet$	deformation gradient
$\mathbf{V}_\bullet \equiv (\mathbf{F}_\bullet \mathbf{F}_\bullet^T)^{1/2}$	left stretch tensor from polar decomposition of $\mathbf{F}_\bullet$
$\mathrm{V}^0(V)$	tissue volume at time 0 (time t)
$V_1^0 = f_1 V^0$	incompressible tissue volume fraction at time 0
$V_2^0 = f_2 V^0 = V^0 - V_1^0$	compressible tissue volume fraction at time 0
$J \equiv det(\mathbf{F}) = V/V^0$	volumetric macroscopic Jacobian
$J_2 = V_2/V_2^0$	volumetric Jacobian for compressible tissue fraction
$\overline{\mathbf{B}_\bullet} = J_\bullet^{-2/3} \cdot \mathbf{F}_\bullet \cdot \mathbf{F}_\bullet^T$	isochoric component of left Cauchy-Green strain tensor
$\mathbf{E}_\bullet = \mathrm{In}(\mathbf{V}_\bullet) = \mathrm{In}(\mathbf{F}_\bullet \mathbf{F}_\bullet^T)^{1/2}$	Hencky strain tensor
$\mathbf{L}_\bullet = \dot{\mathbf{F}}_\bullet \mathbf{F}_\bullet^{-1}$	velocity gradient
$\mathbf{D}_\bullet \equiv sym(\mathbf{L}_\bullet) = (1/2)(\mathbf{L}_\bullet + \mathbf{L}_\bullet^T)$	stretching tensor
$\mathbf{W}_\bullet \equiv skw(\mathbf{L}_\bullet) = (1/2)(\mathbf{L}_\bullet - \mathbf{L}_\bullet^T)$	spin tensor
$\mathbf{T}_A$	Cauchy stress
$\mathbf{T}_h = \frac{1}{3} tr(\mathbf{T}_A) \cdot \underline{\mathbf{1}}$	hydrostatic component of Cauchy stress
$\mathbf{T}_d = \mathbf{T}_A - \frac{1}{3} tr(\mathbf{T}_A) \cdot \underline{\mathbf{1}}$	deviatoric component of Cauchy stress
$\mathbf{T}'_\bullet = \mathbf{T}_\bullet - \frac{1}{3} tr(\mathbf{T}_\bullet) \cdot \underline{\mathbf{1}}$	stress deviator
$\mathbf{N}_\bullet = \frac{\mathbf{T}_\bullet}{\sqrt{tr(\mathbf{T}_\bullet^2)}}$	unit tensor in the direction of stress $\mathbf{T}_\bullet$

The model comprises an elastic network (A) representing the instantaneous response of the tissue and a viscoelastic network (elements (B)–(E)) incorporating the dissipative contributions. Following Lee's decomposition [57], the total deformation gradient $\mathbf{F}$ applied to the tissue may be decomposed as:

$$\mathbf{F} = \mathbf{F}_\mathrm{A} \cdot \mathbf{F}_\mathrm{B}, \tag{1}$$

where $\mathbf{F}_\mathrm{A}$ and $\mathbf{F}_\mathrm{B}$ represent, respectively, the elastic (instantaneous) and viscoelastic components of the tissue deformation. The viscous flow was assumed to be isochoric, hence the total volumetric Jacobian J may be expressed as: $J \equiv \det(\mathbf{F}) = \det(\mathbf{F}_\mathrm{A}) \cdot \det(\mathbf{F}_\mathrm{B}) = \det(\mathbf{F}_\mathrm{A})$. The viscoelastic response of the tissue is captured by the combination of a nonlinear short-term viscous element (B) and a linear viscoelastic backstress network (CDE). With regard to the backstress network, the viscoelastic deformation gradient $\mathbf{F}_\mathrm{B}$ is further decomposed as:

$$\mathbf{F}_\mathrm{B} = \mathbf{F}_\mathrm{C} \cdot \mathbf{F}_\mathrm{D}, \tag{2}$$

where the linear viscous element (D) models the long-term relaxation of the backstress contribution. Both $\mathbf{F}_\mathrm{C}$ and $\mathbf{F}_\mathrm{D}$ are taken to be isochoric.

The Cauchy stress $\mathbf{T}_\mathrm{A}$ in the tissue is decomposed into its hydrostatic and deviatoric components:

$$\mathbf{T}_\mathrm{A} = \mathbf{T}_\mathrm{h} + \mathbf{T}_\mathrm{d}, \tag{3}$$

where the hydrostatic component $\mathbf{T}_\mathrm{h}$ and the deviatoric component $\mathbf{T}_\mathrm{d}$ are physically associated with the deformation mechanisms prevailing in bulk and in shear, i.e. governing the volume-mediated and shear-mediated portions of the tissue response, respectively.

3.2.1. Bulk-mediated response

Brain tissue is highly hydrated. Although interstitial fluid diffusion is not explicitly included in the current model, a simplified qualitative understanding of the role of hydrating fluid in determining the apparent volumetric tissue behavior is the foundation of the proposed formulation for the bulk response. Briefly, the undeformed tissue volume, V^0, is partitioned into an incompressible fraction, $f_1 V^0 = V_1^0$, and a compressible fraction, $f_2 V^0 = V_2^0$, where $f_1 + f_2 = 1$. The corresponding components of the deformed tissue volume, V, are V_1 and V_2. This partition mirrors a separation of the hydrating fluid in a "bound" component, which does not diffuse freely under loading, and an "interstitial" component, which diffuses in response to hydrostatic loading, accommodating volumetric tissue deformation. The incompressible fraction of the volume, V_1, is conserved, so that the corresponding volumetric Jacobian $J_1 = V_1/V_1^0$ remains constant ($J_1 \equiv 1$) throughout the deformation history. The hydrostatic stress $\mathbf{T}_\mathrm{h}$ developed in the tissue is then assumed to be driven by the volumetric Jacobian of the compressible fraction, $J_2 = V_2/V_2^0$, as:

$$\mathbf{T}_\mathrm{h} = K \cdot \ln(J_2) \cdot \underline{\mathbf{1}}, \tag{4}$$

where the hydrostatic stress is characterized by a logarithmic dependence on the volumetric Jacobian and K is the small strain bulk modulus of the compressible fraction. As a consequence of the incompressibility constraint enforced for V_1, the macroscopic tissue volumetric Jacobian $J = V/V^0$ can be expressed as:

$$J = f_1 + (1 - f_1) J_2, \tag{5}$$

so that the hydrostatic stress may be restated in terms of the total volumetric Jacobian J:

$$\mathbf{T}_\mathrm{h} = K \cdot \ln\left[\frac{J - f_1}{1 - f_1}\right] \cdot \underline{\mathbf{1}}. \tag{6}$$

Estimates of typical hydration levels for brain tissue indicate that fluid accounts for approximately 80% of the brain mass [58]. Although the incompressible tissue fraction is effectively a material property, a fixed value $f_1 \approx 0.8$ was selected for the proposed model. This latter assumption is based on the notion that interstitial cerebrospinal fluid, which is free to diffuse throughout the tissue, only accounts for a small portion of the total water content. Phenomenologically, the proposed constitutive framework captures the highly nonlinear resistance to volumetric deformation exhibited by the brain parenchyma. Also, note that in setting the incompressible fraction to 80% the current formulation implicitly assumes that the volumetric response of the tissue becomes infinitely stiff as the volumetric Jacobian approaches 0.8.

3.2.2. Shear-mediated response

The deviatoric component of the stress response, $\mathbf{T}_\mathrm{d}$, is adapted from the freely jointed eight chain model developed for macromolecular elastic networks [59]:

$$\mathbf{T}_\mathrm{d} = \frac{\mu_0}{J} \cdot \frac{\lambda_\mathrm{L}}{\lambda} \cdot \mathscr{L}^{-1}\left(\frac{\lambda}{\lambda_\mathrm{L}}\right) \cdot (\overline{\mathbf{B}}_\mathrm{A} - \lambda^2 \underline{\mathbf{1}}), \tag{7}$$

where

$$
\begin{aligned}
J &= \det(\mathbf{F}) = \det(\mathbf{F}_{\mathrm{A}}),\\
\overline{\mathbf{B}}_{\mathrm{A}} &= J^{-2/3}\cdot\mathbf{F}_{\mathrm{A}}\cdot\mathbf{F}_{\mathrm{A}}^{\mathrm{T}},\\
\lambda^2 &= \frac{1}{3}tr(\overline{\mathbf{B}}_{\mathrm{A}}),\\
\mathscr{L}(\beta) &= \coth(\beta) - \frac{1}{\beta},
\end{aligned}
$$

and μ_0 and λ_{L} are model parameters which scale with the initial shear modulus and the limiting extensibility (locking stretch) of the network. $\mathscr{L}$ denotes the Langevin function. The eight chain model, originally developed for elastomeric materials, is based on statistical mechanics arguments. It assumes a weakly bonded network of randomly oriented chains for which the source of resistance to deformation, i.e. the change in Helmholtz free energy, is mainly governed by changes in configurational entropy of the reorienting chains. The adaptation of this model to brain tissue is motivated by the following considerations.

- The cortex is primarily composed of cells (neurons and glia) whose main constitutive elements are actin filaments, neurofilaments and microtubules [58]. These latter components may be viewed, in a highly simplified representation at the mesoscale level, as a loose "assembly" of randomly oriented "chains" sharing some similarities with the idealized statistical mechanics network envisioned for the eight chain model.
- Preliminary force–displacement measurements performed on individual actin filaments [60] suggest that the use of Langevin statistics may be suitable to account for the nonlinear force–extension curves of these structural components.
- The tissue response, as measured experimentally, exhibits nonlinearities which are well captured by the inverse Langevin function. Further, some empirical evidence collected at the cell level [61] suggests that single neurons share similar nonlinear characteristics.

The time-dependent portion of the tissue deformation is defined via the evolution of the velocity gradient $\mathbf{L}$ imposed on the tissue:

$$
\begin{aligned}
\mathbf{L} = \nabla_{\mathrm{x}}\mathbf{v} = \dot{\mathbf{F}}\cdot\mathbf{F}^{-1} &= \dot{\mathbf{F}}_{\mathrm{A}}\cdot\dot{\mathbf{F}}_{\mathrm{A}}^{-1} + \mathbf{F}_{\mathrm{A}}\cdot\dot{\mathbf{F}}_{\mathrm{B}}\cdot\mathbf{F}_{\mathrm{B}}^{-1}\cdot\mathbf{F}_{\mathrm{A}}^{-1}\\
&= \dot{\mathbf{F}}_{\mathrm{A}}\cdot\mathbf{F}_{\mathrm{A}}^{-1} + \mathbf{F}_{\mathrm{A}}\cdot\mathbf{L}_{\mathrm{B}}\cdot\mathbf{F}_{\mathrm{A}}^{-1} = \mathbf{L}_{\mathbf{A}} + \widetilde{\mathbf{L}}_{\mathrm{B}},
\end{aligned}
\tag{8}
$$

where $\mathbf{L}_{\mathrm{B}} = \dot{\mathbf{F}}_{\mathrm{B}}\cdot\mathbf{F}_{\mathrm{B}}^{-1}$ denotes the viscoelastic velocity gradient in the relaxed (unloaded) configuration and $\widetilde{\mathbf{L}}_{\mathrm{B}} = \mathbf{F}_{\mathrm{A}}\cdot\mathbf{L}_{\mathrm{B}}\cdot\mathbf{F}_{\mathrm{A}}^{-1}$ may be interpreted as the "push forward velocity gradient", i.e. the velocity gradient convected to the current (loaded) configuration (see kinematic map provided in Fig. 6 and Chapter 2 of Holzapfel [62] for more details on push forward tensor operations). The velocity gradient $\widetilde{\mathbf{L}}_{\mathrm{B}}$ may be further decomposed into its symmetric and skew symmetric parts, $\widetilde{\mathbf{L}}_{\mathrm{B}} = \widetilde{\mathbf{D}}_{\mathrm{B}} + \widetilde{\mathbf{W}}_{\mathrm{B}}$, where $\widetilde{\mathbf{D}}_{\mathrm{B}}$ and $\widetilde{\mathbf{W}}_{\mathrm{B}}$ denote the rate of viscous stretch and the viscous spin, respectively. Following [63], the unloaded (relaxed) configuration may be made unique by specifying $\widetilde{\mathbf{W}}_{\mathrm{B}} \equiv 0$, and thus the evolution of the viscoelastic component of the deformation gradient $\mathbf{F}_{\mathrm{B}}$ reduces to: $\dot{\mathbf{F}}_{\mathrm{B}} = \mathbf{F}_{\mathrm{A}}^{-1}\cdot\widetilde{\mathbf{D}}_{\mathrm{B}}\cdot\mathbf{F}$. The viscous stretching tensor $\widetilde{\mathbf{D}}_{\mathrm{B}}$ is constitutively prescribed to follow the direction of the deviator $\mathbf{T}'_{\mathrm{B}}$ of the driving stress $\mathbf{T}_{\mathrm{B}}$ according to a nonlinear reptation-based scaling law, adapted from [64]:

$$
\widetilde{\mathbf{D}}_{\mathrm{B}} = \dot{\gamma}_{\mathrm{B}}\cdot\widetilde{\mathbf{N}}_{\mathrm{B}} = \dot{\gamma}_{\mathrm{B}}\cdot\frac{\mathbf{T}'_{\mathrm{B}}}{\sqrt{tr(\mathbf{T}'^{2}_{\mathrm{B}})}} = \dot{\gamma}_0 f_{\mathrm{R}}\left(\frac{\sqrt{\mathbf{T}'_{\mathrm{B}}:\mathbf{T}'_{\mathrm{B}}}}{\sqrt{2}\sigma_0}\right)^{n}\cdot\frac{\mathbf{T}'_{\mathrm{B}}}{\sqrt{tr(\mathbf{T}'^{2}_{\mathrm{B}})}};
\tag{9}
$$

$$
f_{\mathrm{R}} = \frac{\alpha^2}{\left(\alpha + \sqrt{tr(\mathbf{F}_{\mathrm{B}}\mathbf{F}_{\mathrm{B}}^{\mathrm{T}})/3} - 1\right)^2},
\tag{10}
$$

where $\dot{\gamma}_0$ is a dimensional scaling constant ($\dot{\gamma}_0 = 10^{-4}\ \mathrm{s}^{-1}$). The reptation factor $\mathrm{f_R}$ accounts for the increasing resistance to viscous flow observed in macromolecular networks for increasing levels of accumulated viscous deformation. The factor α is a small constant introduced to eliminate the singularity at $\mathbf{F}_{\mathrm{B}} = 1$ [64], and is set to 0.005. The rate sensitivity exponent n and the strength parameter σ_0 are material properties.

The driving stress $\mathbf{T}_{\mathrm{B}}$ for the (short-term) nonlinear viscous element (B) is obtained as the difference between the Cauchy stress in the tissue $\mathbf{T}_{\mathrm{A}}$ and the backstress from the linear viscoelastic network (CDE) convected to the current configuration:

$$
\mathbf{T}_{\mathrm{B}} = \mathbf{T}_{\mathrm{A}} - \mathbf{T}_{\mathrm{C}} = \mathbf{T}_{\mathrm{A}} - \frac{1}{J}\cdot\mathbf{F}_{\mathrm{A}}\cdot\mathbf{S}_{\mathrm{C}}\cdot\mathbf{F}_{\mathrm{A}}^{\mathrm{T}}.
\tag{11}
$$

The second Piola–Kirchhoff stress, $\mathbf{S}_{\mathrm{C}}$, in the elastic element (C) of the backstress network is taken to scale linearly with the Hencky strain (for a discussion on the adequacy of the Hencky strain measure at finite strains the reader is referred to Anand [65]) of the corresponding deformation gradient $\mathbf{F}_{\mathrm{C}}$:

$$
\mathbf{S}_{\mathrm{C}} = 2G_0\mathbf{E}_{\mathrm{C}} = 2G_0\ln(\mathbf{V}_{\mathrm{C}}) = 2G_0\ln\left(\mathbf{F}_{\mathrm{C}}\mathbf{F}_{\mathrm{C}}^{\mathrm{T}}\right)^{1/2},
\tag{12}
$$

where $\mathbf{E}_{\mathrm{C}}$ is deviatoric, due to the isochoric nature of $\mathbf{F}_{\mathrm{C}}$ [66], and G_0 is a material parameter representing the short-term shear modulus of the viscoelastic backstress network.

A parallel constitutive framework is followed to evaluate the driving stress for the long-term linear viscous element (D), as the difference between the stress $\mathbf{S}_{\mathrm{C}}$ in the elastic element (C) and the long-term backstress $\mathbf{S}_{\mathrm{E}}$ in the elastic element (E):

$$
\mathbf{S}_{\mathrm{D}} = \mathbf{S}_{\mathrm{C}} - \mathbf{F}_{\mathrm{C}}\cdot\mathbf{S}_{\mathrm{E}}\cdot\mathbf{F}_{\mathrm{C}}^{\mathrm{T}},
\tag{13}
$$

where

$$
\mathbf{S}_{\mathrm{E}} = 2G_{\infty}\mathbf{E}_{\mathrm{D}} = 2G_{\infty}\ln(\mathbf{V}_{\mathrm{D}}) = 2G_{\infty}\ln\left(\mathbf{F}_{\mathrm{D}}\mathbf{F}_{\mathrm{D}}^{\mathrm{T}}\right)^{1/2},
\tag{14}
$$

and G_{∞} is a material parameter related to the long-term (equilibrium) shear response of the viscoelastic backstress network. The flow-driven deformation mechanisms unfolding in the tissue at long times are controlled via the linear viscous element (D). The corresponding velocity gradient $\widetilde{\mathbf{L}}_{\mathrm{D}}$ in the elastically unloaded configuration is constitutively prescribed by setting $\widetilde{\mathbf{W}}_{\mathrm{D}} \equiv 0$ and obtaining the stretching tensor, $\widetilde{\mathbf{D}}_{\mathrm{D}} = \mathbf{F}_{\mathrm{C}}\cdot\dot{\mathbf{F}}_{\mathrm{D}}\cdot\mathbf{F}_{\mathrm{B}}^{-1}$, as:

$$
\widetilde{\mathbf{D}}_{\mathrm{D}} = \frac{1}{\sqrt{2}\cdot\eta}\cdot\mathbf{S}_{\mathrm{D}},
\tag{15}
$$

where the viscosity η is a material parameter.

In summary, the proposed large strain kinematics model comprises eight material parameters: K, μ_0, λ_{L}, n, σ_0, G_0, G_{∞} and η. Values of these parameters appropriate to capture the (conditioned) response of brain tissue were determined in the following sections by fitting the proposed model to the measured response in unconfined compression.

3.3. Model fit

The constitutive model was implemented as a Fortran user-defined material subroutine in ABAQUS/Standard (Simulia, Providence, RI). Time integration of the constitutive model was accomplished through an explicit scheme where the viscous stretching tensors were taken to be constant over each time increment. The model was fitted to the conditioned tissue response using the representative set of axial data, i.e. axial data lying about the average, as reported in Figs. 1 and 3, along with the average lateral data shown in Fig. 5D. The fit was initiated using the Nelder–Mead simplex method [67,68] and subsequently optimized manually. The optimized material parameters were found to be:

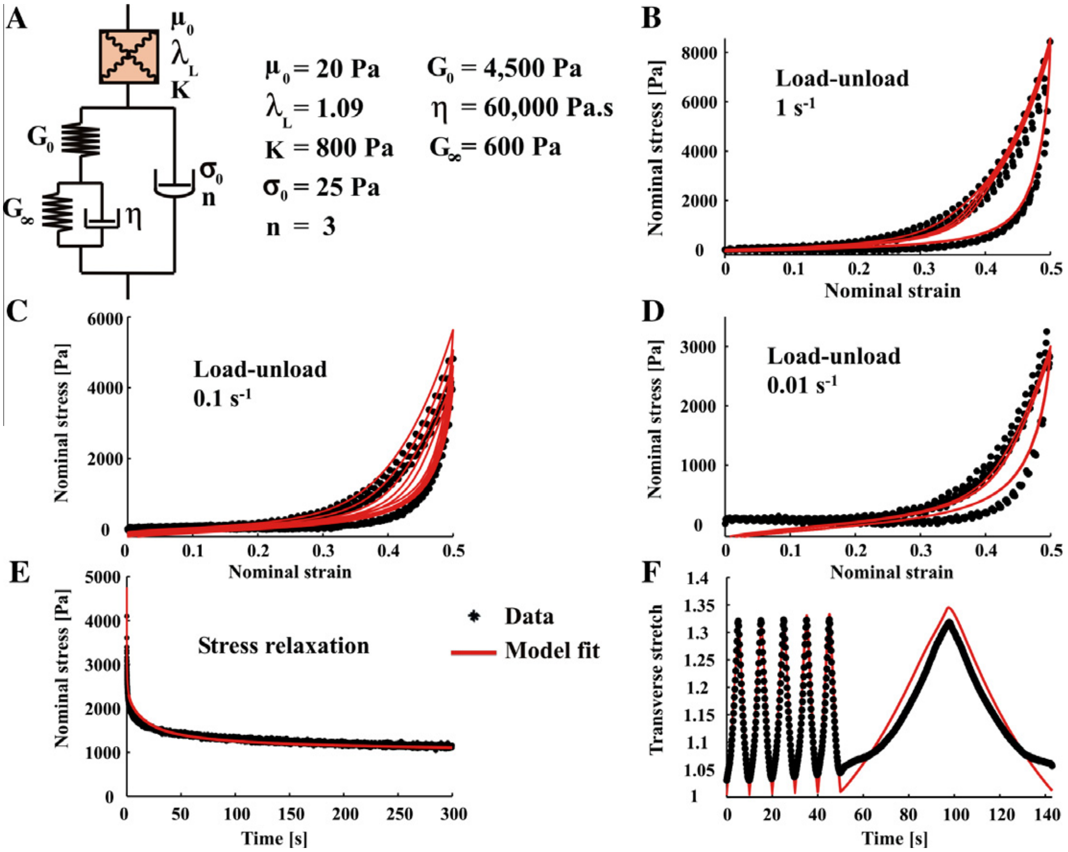

Fig. 7. Model fit to representative data set in unconfined uniaxial compression. (A) Optimized material parameters. (B–E) Axial tissue response (measured and simulated) over the entire loading history. (F) Associated lateral deformation (measured and simulated) over the five load–unload cycles at 0.1 s^{-1} strain rate and the first cycle at 0.01 s^{-1} strain rate. The weighted mean squared error between the simulated and measured responses (see Appendix for details) was found to be 3.5×10^{-3}.

$K = 800$ Pa, $\mu_0 = 20$ Pa, $\lambda_L = 1.09$, $n = 3$, $\sigma_0 = 25$ Pa, $G_0 = 4500$ Pa, $G_\infty = 600$ Pa, $\eta = 60{,}000$ Pa s. For a discussion on the material parameter determination and the automated search algorithm the reader is referred to Appendix A. The optimized simulation results are summarized in Fig. 7. The proposed material formulation successfully captures the main features of the tissue response: volumetric compliance, hysteresis, long-time relaxation behavior and nonlinear strain/strain rate dependencies spanning three orders of strain rate magnitude. Note that the load–unload response at different strain rates and the relaxation response were experimentally obtained (and numerically simulated) over a single sequential loading history. Some discrepancies in material response were encountered between the model and experiment in the low strain rate, low strain regime (Fig. 7C and D). These differences stemmed mainly from the fact that perfect adhesion was assumed in the numerical model between sample and upper platen at all times, whereas, experimentally, contact between the sample and platen was lost at low strains, low rates in the final/initial portion of the unloading/reloading segments. Some artifacts could have been added to the simulation procedure in order to account for these loss of contact effects. However, given the high compliance of the tissue at low strains and low rates, the simpler "perfect adhesion" assumption was deemed sufficient for the purpose of this study.

3.4. Model predictions

To further assess the applicability/relevance of the proposed formulation, the predictions of the proposed model were compared with two sets of data collected, respectively, by Miller and Chinzei [36] (the test conditions and animal model used in the Miller and Chinzei study were nearly identical to the protocols followed in this study, allowing a direct comparison) in uniaxial tension at quasi-static strain rates and by the authors in unconfined uniaxial compression at a 10 s^{-1} strain rate (the compression test protocol employed at 10 s^{-1} strain rate followed that detailed in the preceding section for the lower rates of deformation). The results are reported in Fig. 8. The loading and unloading response predicted by the model in uniaxial compression at 10 s^{-1} strain rate is in good agreement with the experimental data. The responses predicted by the model in tension at low and medium strain rates are also in good agreement with those reported by Miller and Chinzei in the low to medium strain range. At larger strains, however, the tissue response predicted by the model stiffened, as reported previously for other similar biological tissues [69,70], while the response measured by Miller and Chinzei softened. It may be postulated that the softening behavior observed by Miller and Chinzei at large tensile strains reflected the unfolding of failure mechanisms, which, given the delicate nature of brain tissue, are likely to occur within the tissue and/or at the platen interface for high levels of tensile deformation (unfortunately the Miller and Chinzei data did not include unloading and reloading segments, which could have provided a more conclusive interpretation of the tissue response).

4. Discussion

The experimental protocols developed in this study enabled the collection of a large, consistent pool of mechanical data gathered in vitro on macroscopic brain samples at finite strains (0–50%) in the low to medium strain rate regime (0.01–1 s^{-1}). Of particular

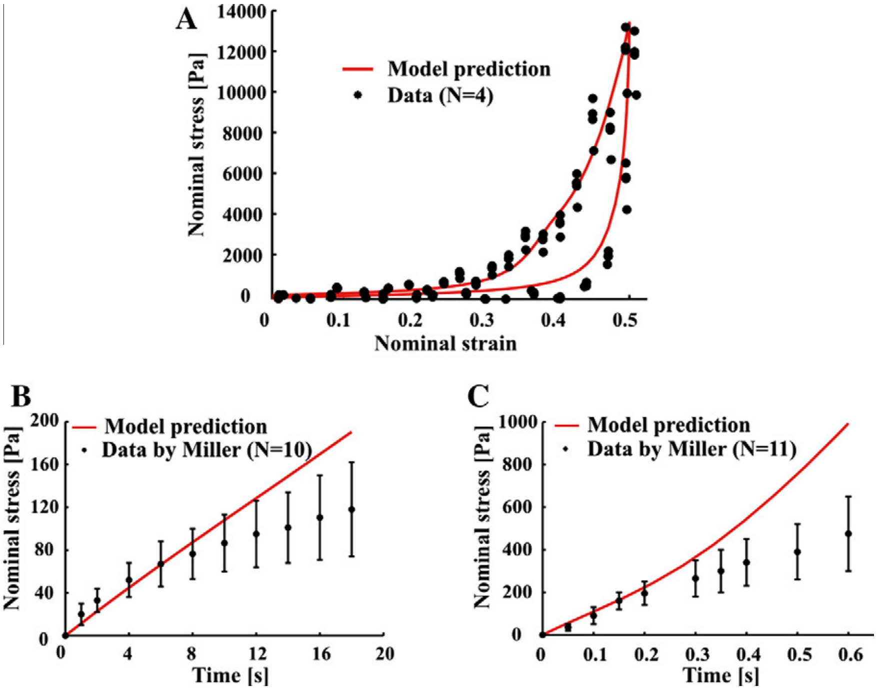

Fig. 8. Model predictions compared with measured responses in unconfined uniaxial compression (A) and uniaxial tension (B and C). (A) Tissue response measured in compression to 50% nominal strain at $10\ \mathrm{s}^{-1}$ strain rate. (B) Average tissue response measured by Miller and Chinzei [36] in tension on 10 mm high specimens to 15% nominal strain at 5 mm min^{-1} ($\sim 0.0083\ \mathrm{s}^{-1}$ nominal strain rate). (C) Average tissue response measured by Miller and Chinzei [36] in tension on 10 mm high specimens to 50% nominal strain at 500 mm min^{-1} ($\sim 0.83\ \mathrm{s}^{-1}$ nominal strain rate).

interest are some quantitative features of the tissue response, e.g. volumetric compliance, large strain viscoelastic behavior upon unloading and reloading and combined nonlinearities in the strain and strain rate domains, which were not available from previous studies but which are highly relevant to guide the development of accurate rheological models. In particular, the experimental measurement of the unloading portion of the tissue response proved crucial in the identification of the relative contributions of elastic and viscoelastic mechanisms to the overall tissue resistance to deformation. The determination of these contributions in the modeling phase enabled the resulting model to predict tissue behavior at a strain rate ($10\ \mathrm{s}^{-1}$) lying outside the original range on which the fit was performed. The current study is only a first step towards the development of a model able to provide accurate predictions for the tissue behavior over arbitrary strain histories. Among the limitations of the study it should be noted that: (1) the tissue behavior was only characterized in one mode of deformation (unconfined uniaxial compression) over a range of strain rates not exceeding $10\ \mathrm{s}^{-1}$; (2) lateral stretch measurements could be accurately obtained only in the lower rate regime (0.01–$0.1\ \mathrm{s}^{-1}$) due to the limited capabilities of the image acquisition system; (3) homogenized measurements may have been affected by partial local discontinuities in the deformation field, as sulci were included (care was taken to exclude results from any samples showing manifest opening/sliding at the sulci and/or inhomogeneous deformation – as attested by the images collected via the visual extensometer system); (4) partial adhesion/decohesion of the specimens from the platens might have affected/altered the measured tissue response at the end of the unloading ramps; (5) the tissue did not reach full equilibrium at the end of the 5 min relaxation period selected for this study, suggesting that relaxation tests where the deformation is held over the course of 20–30 min, i.e. within a time window for which tissue degradation may still be neglected, are needed to measure equilibrium tissue response. Also, note that the conditioned response of the tissue was investigated and characterized according to a decreasing order of deformation rates. Preliminary results (unpublished) seem to indicate that once a sample was deformed at a given rate it was "conditioned" for deformation at that rate and at lower rates but it would still exhibit additional conditioning if tested subsequently at higher rates. Altering the order of the loading segments in future studies may, therefore, provide useful validation data for a model accounting for conditioning effects.

The proposed constitutive model successfully captures the main features of the large strain tissue response, as measured in uniaxial compression and tension. While the selected set of material parameters was optimized specifically for the conditioned tissue

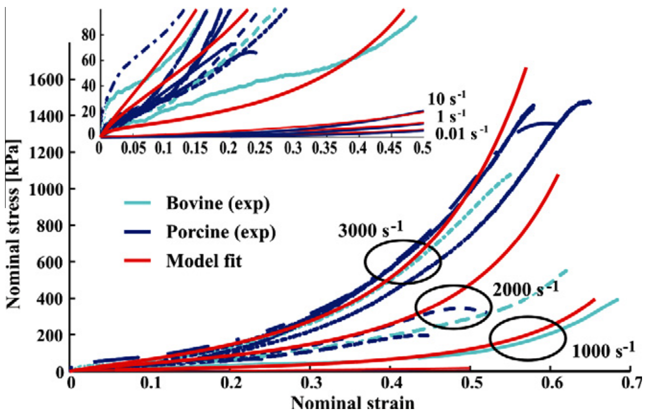

Fig. 9. Model fit to the tissue response measured upon loading in unconfined uniaxial compression at nominal strain rates spanning six orders of magnitude (0.001–$3000\ \mathrm{s}^{-1}$). The sets of bovine and porcine data reported at high rates (1000–$3000\ \mathrm{s}^{-1}$) were obtained by the Chen group at Purdue University via Kolsky bar measurements [7]; the porcine data shown for the low to medium strain rates (0.001–$10\ \mathrm{s}^{-1}$) are those collected by the authors. The optimized model parameters for the fit are: $K = 10$ MPa; $\mu_0 = 10$ kPa; $\lambda_L = 1.03$, $n = 0.3$; $\sigma_0 = 2$ kPa; $G_0 = 6$ kPa; $G_\infty = 2$ kPa; $\eta = 1$ kPa s. The dimensional factor $\dot{\gamma}_0$ was set to $1000\ \mathrm{s}^{-1}$ and the reptation factor f_R to 1.

response in the low to medium strain rate regime, the current formulation remains general in nature and might be applied to model tissue responses over more extensive ranges of strain rates (the proposed formulation was also found to be appropriate to model the response of rat neurons as measured via atomic force microscopy (AFM) indentation [61]). To demonstrate this versatility, a preliminary fit of the model to the unconditioned (first loading ramp) tissue response measured at low to high rates of deformation (0.01–3000 s^{-1}) was conducted. The main results are reported in Fig. 9. The set of material parameters found to capture the tissue response upon loading at high rates was: $K = 10$ MPa, $\mu_0 = 10$ kPa, $\lambda_L = 1.03$, $n = 0.3$, $\sigma_0 = 2$ kPa, $G_0 = 6$ kPa, $G_\infty = 2$ kPa, $\eta = 1$ kPa s. Note that to capture the high rate regime response the material parameters needed to be altered. This is to be expected, as additional mechanisms of resistance to deformation might be operative at these rates. This observation mirrors findings in polymeric materials [71], where additional constitutive elements are required to account for the increased resistance to molecular motions in the high frequency regime. The bulk response of biological materials was also found to be substantially stiffer at high rates of deformation [72], as diffusion of interstitial fluid was drastically reduced. The proposed model, with the modified material parameters reported in Fig. 9, efficiently captures the essential features of the unconditioned loading response of brain tissue over a range of strain rates from 0.01 to 3000 s^{-1}. While some of the fine details of the tissue response in the very low rate regime were unavoidably lost with this alternative set of parameters, the extensive range of strains and strain rates over which the tissue response was adequately captured highlights the potential value of this model for finite element simulations of loading transients leading to traumatic brain injury. Typical deformation histories of brain tissue under blunt impact or blast loading conditions present a very wide spectrum of strains and strain rates, with inhomogeneous fields characterized by steep spatial and temporal gradients. The availability of an accurate constitutive law to model the brain tissue response is a crucial requirement to assess local levels of strain, stress and strain rate associated with potential injury mechanisms. The proposed model represents a first step towards the attainment of this goal. Further model refinements are needed to address the time dependence of the volumetric response associated with the

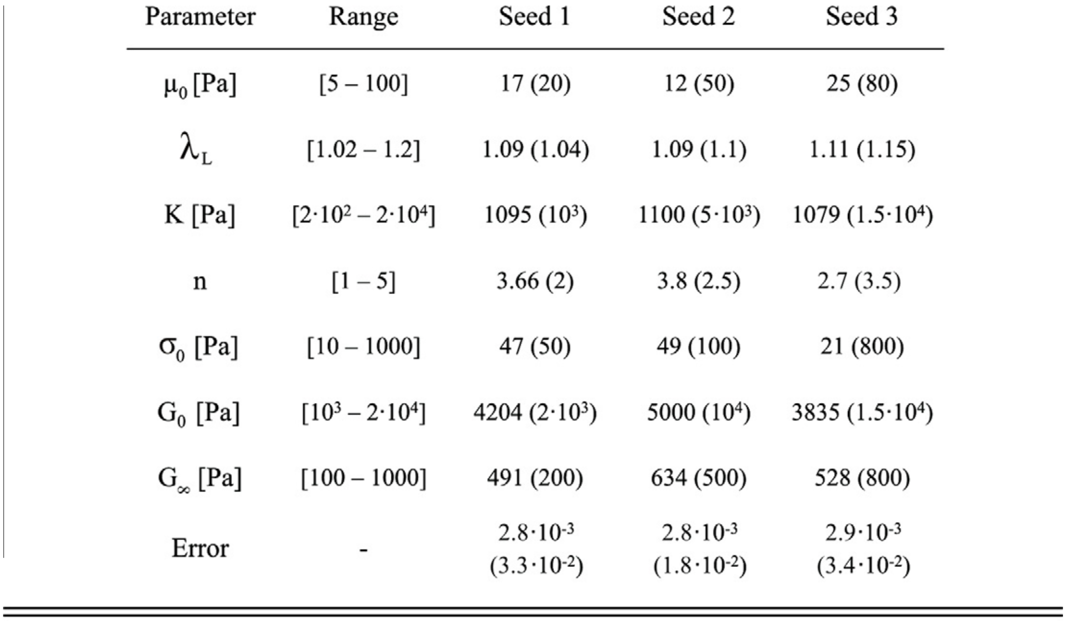

Parameter	Range	Seed 1	Seed 2	Seed 3
μ_0 [Pa]	[5 – 100]	17 (20)	12 (50)	25 (80)
λ_L	[1.02 – 1.2]	1.09 (1.04)	1.09 (1.1)	1.11 (1.15)
K [Pa]	[$2\cdot10^2$ – $2\cdot10^4$]	1095 (10^3)	1100 ($5\cdot10^3$)	1079 ($1.5\cdot10^4$)
n	[1 – 5]	3.66 (2)	3.8 (2.5)	2.7 (3.5)
σ_0 [Pa]	[10 – 1000]	47 (50)	49 (100)	21 (800)
G_0 [Pa]	[10^3 – $2\cdot10^4$]	4204 ($2\cdot10^3$)	5000 (10^4)	3835 ($1.5\cdot10^4$)
G_∞ [Pa]	[100 – 1000]	491 (200)	634 (500)	528 (800)
Error	-	$2.8\cdot10^{-3}$ ($3.3\cdot10^{-2}$)	$2.8\cdot10^{-3}$ ($1.8\cdot10^{-2}$)	$2.9\cdot10^{-3}$ ($3.4\cdot10^{-2}$)

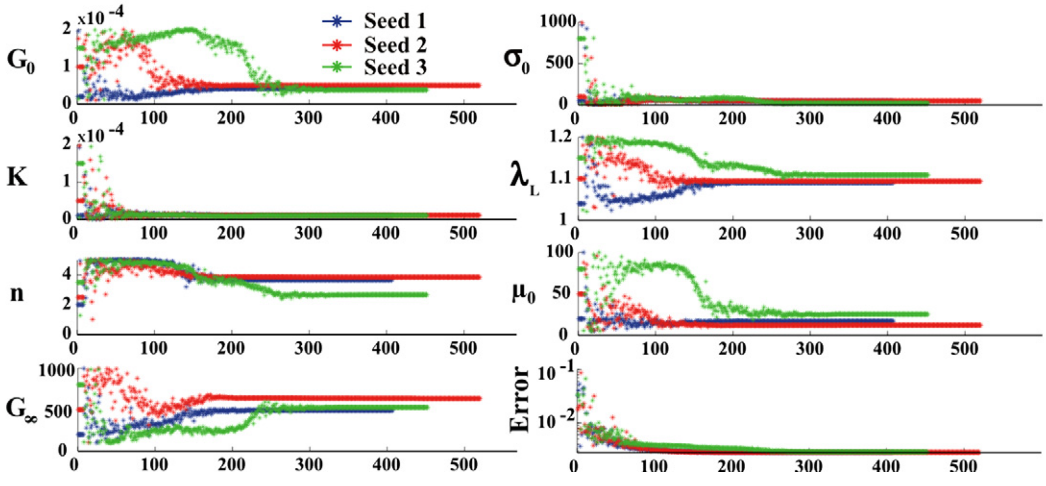

Fig. 10. A summary of the parameter search results obtained from three independent parameter seeds (starting guesses) using the simplex optimization method. The experimental data used for the automated fitting procedure were the representative sets of axial and lateral measurements provided in Figs. 3 and 5D, respectively. For each seed (top table) the converged parameter values are reported, along with the corresponding starting seed in parentheses. The range indicated for each material parameter corresponds to the investigation domain over which the automated algorithm was allowed to search for minima. The material parameter and error function evolutions for the search procedure are shown in the bottom graphs (iteration numbers reported on the x-axis).

biphasic nature of the tissue in the high to intermediate strain rate regime.

5. Conclusions

This study presents a significant pool of in vitro experimental results collected on porcine cortical brain tissue in unconfined compression up to 50% nominal strain over three orders of strain rate magnitude (0.01–1 s^{-1}), both under in load/unload cycles, with quantitative assessments of the tissue lateral deformation. The constitutive model presented here successfully captures the complex features inherent in the tissue response (hysteresis, nonlinearities, volumetric compliance, short- and long-time behaviors) over four orders of strain rate magnitude (0.01–10 s^{-1}), up to 50% nominal strain with a relatively low number of material parameters. The model is also able to predict the tissue behavior in tension at quasi-static rates ($\sim 0.83 \times 10^{-2}$–$0.83\ s^{-1}$) up to ~20% strain. Further testing of the ability of the model to predict the material response under different modes of deformation is a necessary future step. While the results of previous studies on the shear behavior of the tissue are available in the literature [15,23,37], variations in experimental protocols (post mortem time, age and species of the animal model, sample size, orientation, composition, tissue conditioning, etc.) led to large relative discrepancies. In order to circumvent these difficulties, an experimental investigation of the shear response of comparable tissue samples under testing conditions identical to those of the current study would be needed to assess the ability of the current version of the model to capture the material response in simple shear. Furthermore, an experimental and computational investigation of the tissue response to dynamic indentation is being conducted to better characterize the accuracy of the model for inhomogeneous deformations and complex boundary conditions. Finally, the current formulation does not account for the observed conditioning effects, where the first loading ramp was associated with a substantially stiffer tissue response. Interstitial fluid diffusion may play a significant role in this conditioning process and future model refinements would need to account for these poro-elastic effects.

Acknowledgements

The authors acknowledge the support of the US Army Research Office, through the MIT Institute for Soldier Nanotechnologies (W911NF-07-D-0004) and the Joint Improvised Explosive Devices Defeat Organization (W911NF-07-1-0035), and that of École Nationale des Ponts et Chaussées (Université Paris-Est, France). Partial support for this work was also obtained from the Computational Systems Biology Programme of the Singapore–MIT Alliance and from the Interdisciplinary Research Group on Infectious Diseases, funded by the Singapore–MIT Alliance for Research and Technology Centre. The authors are grateful to Professor Wayne Chen from Purdue University for providing the high rate tissue data. There is no conflict of interest to be reported.

Appendix A

A.1. Determination of material parameters

The eight material parameters to be determined for the current model are: K for the overall bulk response; μ_0 and λ_L for the elastic shear response of network (A); G_0, G_∞ and η for the linear

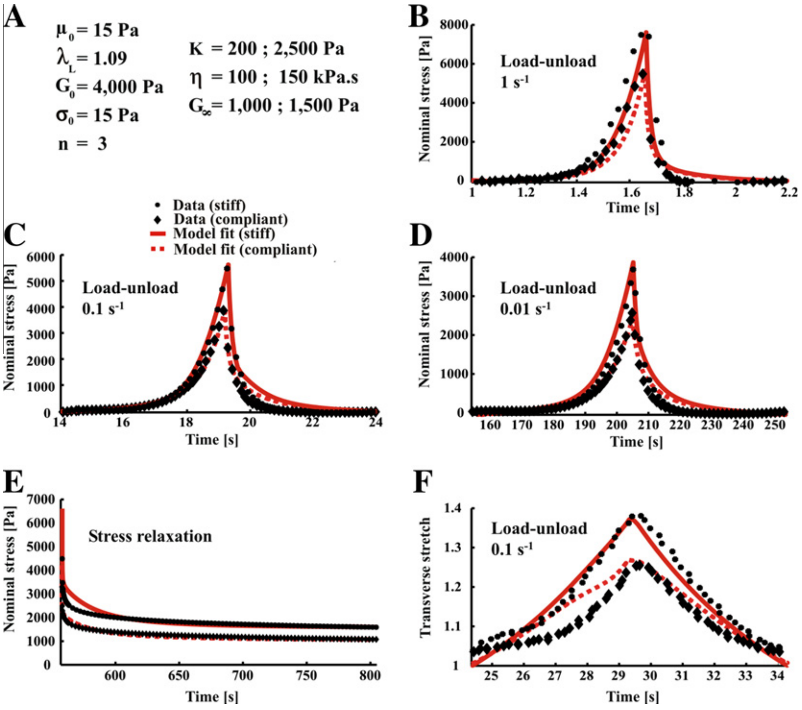

Fig. 11. Model fit to responses measured in unconfined uniaxial compression from two "outlying" samples whose axial stresses and lateral stretches developed upon loading at large strains deviated from average by about plus and minus one standard deviation (labeled as "stiff" and "compliant", respectively). (A) Optimized material parameters. Only K, G_∞, and η differed between the two outliers (stiff/compliant). The low and high values provided for each of these latter parameters corresponded to those associated with the compliant and stiff responses, respectively. (B–E) Axial tissue responses (measured and simulated) for both outlying cases. (F) Associated lateral deformations (measured and simulated). For clarity purposes, only the second load–unload segments are provided for each strain rate (at a decreased sampling rate). The weighted mean squared errors between the responses simulated and measured over the entire loading history (see Appendix for error definition) were found to be 3.3×10^{-3} (stiff) and 4.8×10^{-3} (compliant).

viscoelastic backstress network (CDE); σ_0 and n for the reptation-based short-term viscous response.

A.2. Preliminary parameter estimate

The following considerations were used to narrow down the search range for appropriate parameter values.

1. Estimates for μ_0 and λ_L may be obtained by considering the slope of the uniaxial stress–strain curve at the onset of deformation and the instantaneous (elastic) slope upon unloading at maximum strain; μ_0 correlates with the initial shear response and λ_L correlates with the limiting stretch for tissue extensibility. An initial guess for μ_0 falling in the range 5–100 Pa was found to be appropriate. In order to match the steep unloading response observed in the experimental data, initial guesses for λ_L were selected to be in the range 1.02–1.2.
2. The (small strain) bulk modulus K may be estimated by examination of the lateral stretch data. The measured stress–strain response, in conjunction with the lateral stretch data can be used to obtain pressure volumetric Jacobian plots of the measured tissue response, from which an appropriate range for the bulk modulus may be obtained. In practice, an initial guess for K lying in the range 200–20,000 Pa was found to be appropriate.
3. G_∞ and η govern the long-term viscoelastic response of the tissue; their ratio η/G_∞, scaling with the long-term relaxation time of the tissue, was estimated to be about 100 s upon inspection of the long-term relaxation responses. η was thus set to $100 \cdot G_\infty$ for the parameter search. Also based on the long-term equilibrium response, an initial guess for G_∞ was determined to fall in the range 100–1000 Pa. G_0, which must be held sufficiently high to sustain a prompt reversal of the viscous flow at high rates but also sufficiently low to prevent any excessive stiffening at large strains and low rates, was estimated to fall in the range 1–20 kPa.
4. σ_0 and n modulate the onset of deformation in the nonlinear viscous element and the nonlinear strain rate sensitivity of the tissue, respectively. In the experimental data collected for this study the tissue exhibited substantial rate sensitivity, so that initial guesses for the exponential coefficient n were set in the range 1–5. As viscous flow was experimentally observed at low stress levels, initial guesses for the strength parameter σ_0 were kept below 1 kPa, with initial estimates in the range 10–1000 Pa.

A.3. Automated parameter search algorithm

Based on these preliminary considerations, a systematic automated search was conducted using the Nelder–Mead simplex algorithm [67,68] implemented in a MATLAB subroutine. The seven variable (μ_0, λ_L, K, G_∞, G_0, σ_0, n) error function minimized via the search algorithm was defined in terms of a weighted mean squared difference between the experimental and modeled stress and lateral stretch histories:

$$\text{error} = \frac{1}{|S_{\text{exp}}^{\max}|} \cdot ||w_s \cdot (s_{\text{exp}} - s_{\text{model}})|| + \gamma \cdot ||w_\lambda \cdot (\lambda_{\text{exp}} - \lambda_{\text{model}})||$$

where $||\ ||$ is the Euclidian norm, s_{exp} and λ_{exp} and s_{model} and λ_{model} are the discrete time nominal stress and lateral stretch vectors obtained experimentally and numerically, respectively; $|S_{\text{exp}}^{\max}|$ is a normalization factor equal to the peak nominal stress value at 1 s^{-1} strain rate, γ is a bias factor discussed hereafter and w_s and w_λ are weighting vectors designed to increase the significance of the tissue response as the strains/stresses grow larger:

$$w_s[i] = \frac{1}{\sum_j w_s[j]} \cdot \left(1 + \left|\frac{S_{\text{exp}}[i]}{S_{\text{exp}}^{\max}}\right|\right)$$

$$w_\lambda[i] = \frac{1}{\sum_j w_\lambda[j]} \cdot \left(1 + 10^5 \cdot |\lambda_{\text{exp}}[i] - \lambda_{\text{exp}}[0]|\right)$$

The discrete lateral stretch vector λ_{exp} was sampled from the portion of the response for which reliable volumetric measurements were available, i.e. over the five load–unload cycles at 0.1 s^{-1} and the first load–unload cycle at 0.01 s^{-1}. The weighting factor γ modulating the lateral deformation portion of the error function was set to 2 to compensate for the diminished pool of available lateral stretch data.

Upon starting the simplex minimization scheme the user provides an initial guess for the seven material parameters, along with lower and upper bounds for each of them. Note that this direct search method does not necessarily converge to a minimizing point. The algorithm was therefore run repeatedly, starting from various initial guesses selected within the ranges determined via the preliminary parameter estimate. The search results are shown for one representative set of seed points in Fig. 10. The automated search provided a remarkably consistent set of material parameters. The latter parameter estimates were slightly readjusted manually to capture subtle features of the response (e.g. nonlinear behavior in the low strain range, volumetric compliance at large strains) that the global error measure employed for the optimization search procedure could not specifically account for. The mean squared error obtained via the supplementary manual fit was of the same order as that found via the automated search, i.e. $\sim 3.5 \times 10^{-3}$. The final selected set of material parameters is reported in Fig. 7.

A.4. Parameter estimates for "outlying" cases

Using the parameter estimates obtained for the average tissue response as the baseline, additional fits were performed manually to assess the sensitivity of the material parameters to deviations from the average tissue response. Two "extreme" cases were selected – termed "stiff" and "compliant" – for which the axial stresses and lateral stretches measured upon loading in the large strain regime deviated from the average by about plus and minus one standard deviation, respectively. The results are reported in Fig. 11. The most prominent differences in material response could be accounted for by altering the bulk parameter and long-term viscous coefficients while retaining the remaining parameters virtually unchanged.

References

[1] Estes MS, McElhaney JH. Response of brain tissue to compressive loading. Mech Eng 1970;92:58–61.

[2] Pamidi MR, Advani SH. Nonlinear constitutive relations for human brain tissue. J Biomech Eng Trans ASME 1978;100:44–8.

[3] Mendis KK, Stalnaker RL, Advani SH. A constitutive relationship for large deformation finite element modeling of brain tissue. J Biomech Eng Trans ASME 1995;117:279–85.

[4] Miller K. Constitutive model of brain tissue suitable for finite element analysis of surgical procedures. J Biomech 1999;32:531–7.

[5] Takhounts EG, Crandall JR, Darvish K. On the importance of nonlinearity of brain tissue under large deformations. Stapp Car Crash J 2003;47:79–92.

[6] Cheng S, Bilston LE. Unconfined compression of white matter. J Biomech 2007;40:117–24.

[7] Pervin F, Chen WW. Dynamic mechanical response of bovine gray matter and white matter brain tissues under compression. J Biomech 2009;42:731–5.

[8] Zhang LY, Yang KH, King AI. Comparison of brain responses between frontal and lateral impacts by finite element modeling. J Neurotrauma 2001;18:21–30.

[9] Zhang L, Bae J, Hardy WN, Monson KL, Manley GT, Goldsmith W, et al. Computational study of the contribution of the vasculature on the dynamic response of the brain. Stapp Car Crash J 2002;46:145–63.

[10] El Sayed T, Mota A, Fraternali F, Ortiz M. Biomechanics of traumatic brain injury. Comput Methods Appl Mech Eng 2008;197:4692–701.
[11] Brands DWA, Bovendeerd PHM, Wismans JSHM. On the potential importance of non-linear viscoelastic material modelling for numerical prediction of brain tissue response: test and application. Stapp Car Crash J 2002;46:103–21.
[12] Zhang LY, Yang KH, King AI. A proposed injury threshold for mild traumatic brain injury. J Biomech Eng Trans ASME 2004;126:226–36.
[13] Gefen A, Gefen N, Zhu QL, Raghupathi R, Margulies SS. Age-dependent changes in material properties of the brain and braincase of the rat. J Neurotrauma 2003;20:1163–77.
[14] Arbogast KB, Margulies SS. Material characterization of the brainstem from oscillatory shear tests. J Biomech 1998;31:801–7.
[15] Prange MT, Margulies SS. Regional, directional, and age-dependent properties of the brain undergoing large deformation. J Biomech Eng Trans ASME 2002;124:244–52.
[16] Velardi F, Fraternali F, Angelillo M. Anisotropic constitutive equations and experimental tensile behavior of brain tissue. Biomech Model Mechanobiol 2006;5:53–61.
[17] Metz H, McElhaney J, Ommaya AK. A comparison of the elasticity of live, dead, and fixed brain tissue. J Biomech 1970;3:453–8.
[18] Walsh EK, Furniss WW, Schettini A. On measurement of brain elastic response in vivo. Am J Physiol Regul Integr Comp Physiol 1977;232:27–30.
[19] Miller K, Chinzei K, Orssengo G, Bednarz P. Mechanical properties of brain tissue in-vivo: experiment and computer simulation. J Biomech 2000;33:1369–76.
[20] Gefen A, Margulies SS. Are in vivo and in situ brain tissues mechanically similar? J Biomech 2004;37:1339–52.
[21] Atay SM, Kroenke CD, Sabet A, Bayly PV. Measurement of the dynamic shear modulus of mouse brain tissue in vivo by magnetic resonance elastography. J Biomech Eng Trans ASME 2008;130:021013.
[22] Franceschini G, Bigoni D, Regitnig P, Holzapfel GA. Brain tissue deforms similarly to filled elastomers and follows consolidation theory. J Mech Phys Solids 2006;54:2592–620.
[23] Hrapko M, van Dommelen JAW, Peters GWM, Wismans JSHM. The mechanical behaviour of brain tissue: large strain response and constitutive modelling. Biorheology 2006;43:623–36.
[24] El Sayed T, Mota A, Fraternali F, Ortiz M. A variational constitutive model for soft biological tissues. J Biomech 2008;41:1458–66.
[25] Moore DF, Jerusalem A, Nyein M, Noels L, Jaffee MS, Radovitzky RA. Computational biology – modeling of primary blast effects on the central nervous system. Neuroimage 2009;47:T10–20.
[26] Balakrishnan A, Socrate S. Material property differentiation in indentation testing using secondary sensors. Exp Mech 2008;48:549–58.
[27] Fallenstein GT, Hulce VD, Melvin JW. Dynamic mechanical properties of human brain tissue. J Biomech 1969;2:217–26.
[28] Shuck LZ, Advani SH. Rheological response of human brain tissue in shear. J Basic Eng 1972;94:905–11.
[29] Bilston LE, Liu ZZ, Phan-Thien N. Linear viscoelastic properties of bovine brain tissue in shear. Biorheology 1997;34:377–85.
[30] Nicolle S, Lounis M, Willinger R, Palierne JF. Shear linear behavior of brain tissue over a large frequency range. Biorheology 2005;42:209–23.
[31] Thibault KL, Margulies SS. Age-dependent material properties of the porcine cerebrum: effect on pediatric inertial head injury criteria. J Biomech 1998;31:1119–26.
[32] Peters GWM, Meulman JH, Sauren A. The applicability of the time/temperature superposition principle to brain tissue. Biorheology 1997;34:127–38.
[33] Nicolle S, Lounis M, Willinger R. Shear properties of brain tissue over a frequency range relevant for automotive impact situations: new experimental results. Stapp Car Crash J 2004;48:239–58.
[34] Miller K, Chinzei K. Constitutive modelling of brain tissue: experiment and theory. J Biomech 1997;30:1115–21.
[35] Tamura A, Hayashi S, Watanabe I, Nagayama K, Matsumoto T. Mechanical characterization of brain tissue in high-rate compression. J Biomech Sci Eng 2007;2:115–26.
[36] Miller K, Chinzei K. Mechanical properties of brain tissue in tension. J Biomech 2002;35:483–90.
[37] Darvish KK, Crandall JR. Nonlinear viscoelastic effects in oscillatory shear deformation of brain tissue. Med Eng Phys 2001;23:633–45.
[38] McElhaney JH, Melvin JW, Roberts VL, Portnoy HD. Dynamic characteristics of the tissues of the head. In: Kenedi RM, editor. Perspectives in biomedical engineering. London: The Macmillan Press; 1973. p. 215–22.
[39] Guillaume A, Osmont D, Gaffie D, Sarron JC, Quandieu P. Effects of perfusion on the mechanical behavior of the brain exposed to hypergravity. J Biomech 1997;30:383–9.
[40] Ruan JS, Khalil T, King AI. Dynamic response of the human head to impact by three-dimensional finite element analysis. J Biomech Eng Trans ASME 1994;116:44–50.
[41] Bilston LE, Liu ZZ, Phan-Thien N. Large strain behaviour of brain tissue in shear: some experimental data and differential constitutive model. Biorheology 2001;38:335–45.
[42] Dickerson JWT, Dobbing J. Prenatal and postnatal growth and development of the central nervous system of the pig. Proc R Soc Lond B Biol Sci 1967;166:384–95.
[43] Pampiglione G. Some aspects of development of cerebral function in mammals. Proc R Soc Med Lond 1971;64:429–35.
[44] Flynn TJ. Developmental changes of myelin-related lipids in brain of miniature swine. Neurochem Res 1984;9:935–45.
[45] Duhaime AC, Margulies SS, Durham SR, O'Rourke MM, Golden JA, Marwaha S, et al. Maturation-dependent response of the piglet brain to scaled cortical impact. J Neurosurg 2000;93:455–62.
[46] Fang MR, Li JC, Gong XY, Antonio G, Lee F, Kwong WH, et al. Myelination of the pig's brain: a correlated MRI and histological study. Neurosignals 2005;14:102–8.
[47] Coats B, Margulies SS. Material properties of porcine parietal cortex. J Biomech 2006;39:2521–5.
[48] Balakrishnan A. Development of novel dynamic indentation techniques for soft tissue applications. PhD thesis, Massachusetts Institute of Technology, Cambridge, MA; 2007.
[49] Biot MA. General theory of three-dimensional consolidation. J Appl Phys 1941;12:155–64.
[50] Nicholson C. Diffusion and related transport mechanisms in brain tissue. Rep Prog Phys 2001;64:815–84.
[51] Basser PJ. Interstitial pressure, volume, and flow during infusion into brain tissue. Microvasc Res 1992;44:143–65.
[52] Galford JE, McElhaney JH. A viscoelastic study of scalp, brain, and dura. J Biomech 1970;3:211–21.
[53] Donnelly BR, Medige J. Shear properties of human brain tissue. J Biomech Eng Trans ASME 1997;119:423–32.
[54] Kleiven S, Hardy WN. Correlation of an FE model of the human head with local brain motion – consequences for injury prediction. Stapp Car Crash J 2002;46:123–44.
[55] Brands DWA, Peters GWM, Bovendeerd PHM. Design and numerical implementation of a 3-D non-linear viscoelastic constitutive model for brain tissue during impact. J Biomech 2004;37:127–34.
[56] Kohandel M, Sivaloganathan S, Tenti G, Drake JM. The constitutive properties of the brain parenchyma Part 1. Strain energy approach. Med Eng Phys 2006;28:449–54.
[57] Lee EH. Elastic–plastic deformation at finite strains. J Appl Mech 1969;36:1–6.
[58] Lodish H, Berk A, Kaiser CA, Krieger M, Scott MP, Bretscher A, et al. Molecular cell biology. New York: W.H. Freeman and Co.; 2007.
[59] Arruda EM, Boyce MC. A three-dimensional constitutive model for the large stretch behavior of rubber elastic materials. J Mech Phys Solids 1993;41:389.
[60] Gardel ML, Nakamura F, Hartwig JH, Crocker JC, Stossel TP, Weitz DA. Prestressed F-actin networks cross-linked by hinged filamins replicate mechanical properties of cells. Proc Natl Acad Sci USA 2006;103:1762–7.
[61] Bernick K, Prevost T, Socrate S, Suresh S. Mechanical response of rat cortical neurons: AFM indentations and preliminary modeling. In: Proceedings of the ASME 2009 summer bioengineering conference, Lake Tahoe, CA; 2009.
[62] Holzapfel GA. Nonlinear solid mechanics: a continuum approach for engineering. Chichester, UK: John Wiley & Sons; 2000.
[63] Boyce MC, Weber GG, Parks DM. On the kinematics of finite strain plasticity. J Mech Phys Solids 1989;37:647–65.
[64] Bergstrom JS, Boyce MC. Constitutive modeling of the time-dependent and cyclic loading of elastomers and application to soft biological tissues. Mech Mater 2001;33:523–30.
[65] Anand L. On H. Hencky's approximate strain–energy function for moderate deformations. J Biomech Eng Trans ASME 1979;46:78–82.
[66] Criscione JC. Direct tensor expression for natural strain and fast, accurate approximation. Comput Struct 2002;80:1895–905.
[67] Lagarias JC, Reeds JA, Wright MH, Wright PE. Convergence properties of the Nelder–Mead simplex method in low dimensions. SIAM J Optim 1998;9:112–47.
[68] Jordan P, Socrate S, Zickler TE, Howe RD. Constitutive modeling of porcine liver in indentation using 3D ultrasound imaging. J Mech Behav Biomed Mater 2009;2:192–201.
[69] Chui C, Kobayashi E, Chen X, Hisada T, Sakuma I. Transversely isotropic properties of porcine liver tissue: experiments and constitutive modelling. Med Biol Eng Comput 2007;45:99–106.
[70] Shreiber DI, Hao HL, Elias RAI. Probing the influence of myelin and glia on the tensile properties of the spinal cord. Biomech Model Mechanobiol 2009;8:311–21.
[71] Mulliken AD, Boyce MC. Mechanics of the rate-dependent elastic–plastic deformation of glassy polymers from low to high strain rates. Int J Solids Struct 2006;43:1331–56.
[72] Saraf H, Ramesh KT, Lennon AM, Merkle AC, Roberts JC. Mechanical properties of soft human tissues under dynamic loading. J Biomech 2007;40:1960–7.